

SHEDDING LIGHT ON THE COMPTON-THICK ACTIVE GALACTIC NUCLEUS IN THE ULTRA-LUMINOUS INFRARED GALAXY UGC 5101 WITH BROADBAND X-RAY SPECTROSCOPY

SAEKO ODA¹, ATSUSHI TANIMOTO¹, YOSHIHIRO UEDA¹, MASATOSHI IMANISHI^{2,3,4}, YUICHI TERASHIMA⁵, CLAUDIO RICCI^{6,7}

¹Department of Astronomy, Kyoto University, Kyoto 606-8502, Japan

²Subaru Telescope, 650 North A'ohoku Place, Hilo, HI 96720, USA

³National Astronomical Observatory of Japan, 2-21-1 Osawa, Mitaka, Tokyo 181-8588, Japan

⁴Department of Astronomy, School of Science, Graduate University for Advanced Studies (SOKENDAI), Mitaka, Tokyo 181-8588, Japan

⁵Department of Physics, Ehime University, Bunkyo-cho, Matsuyama, Ehime 790-8577, Japan

⁶Instituto de Astrofísica, Pontificia Universidad Católica de Chile, Casilla 306, Santiago 22, Chile

⁷Kavli Institute for Astronomy and Astrophysics, Peking University, Beijing 100871, China

Draft version November 7, 2018

ABSTRACT

We report the broadband X-ray spectra of the ultra-luminous infrared galaxy (ULIRG) UGC 5101 in the 0.25–100 keV band observed with *Swift*/Burst Alert Telescope (BAT), *NuSTAR*, *Suzaku*, *XMM-Newton*, and *Chandra*. A Compton-thick AGN obscured with a hydrogen column density of $\approx 1.3 \times 10^{24} \text{ cm}^{-2}$ is detected above 10 keV. A spectral fit with a numerical torus model favors a large half opening angle of the torus, > 41 degrees, suggesting that the covering fraction of material heavily obscuring the X-ray source is moderate. The intrinsic 2–10 keV luminosity is determined to be $\approx 1.4 \times 10^{43} \text{ erg s}^{-1}$, which is ≈ 2.5 times larger than the previous estimate using only data below 10 keV with a simple spectral model. We find that UGC 5101 shows the ratio between the [O IV] 26 μm line and 2–10 keV luminosities similar to those of normal Seyfert galaxies, along with other ULIRGs observed with *NuSTAR*, indicating that a significant portion of local ULIRGs are not really “X-ray faint” with respect to the flux of forbidden lines originating from the narrow line region (NLR). We propose a possible scenario that (1) the AGN in UGC 5101 is surrounded not only by Compton-thick matter located close to the equatorial plane but also by Compton-thin ($N_{\text{H}} \sim 10^{21} \text{ cm}^{-2}$) matter in the torus-hole region and (2) it is accreting at a high Eddington rate with a steep UV to X-ray spectral energy distribution. Nevertheless, we argue that AGNs in many ULIRGs do not look extraordinary (i.e., extremely X-ray faint), as suggested by recent works, compared with normal Seyferts.

Subject headings: galaxies: active – galaxies: individual (UGC 5101) – X-rays: galaxies

1. INTRODUCTION

Ultra-luminous infrared galaxies (ULIRGs) radiate the bulk of their large luminosities ($L > 10^{12} L_{\odot}$) as dust emission. This indicates that powerful energy sources, starbursts and/or active galactic nuclei (AGNs), are hidden behind dust. ULIRGs are dominant contributors to the cosmic infrared radiation density at $z > 1.5$ (Caputi et al. 2007, Goto et al. 2010, Murphy et al. 2011). Thus, distinguishing the energy sources in ULIRGs is critical to unveil the history of star-formation and SMBH mass growth in the dust-obscured galaxy population of the early universe. ULIRGs are major mergers of gas-rich galaxies and have large amounts of concentrated molecular gas and dust in their nuclei (Sanders & Mirabel 1996). Hard X-ray ($E > 10 \text{ keV}$) observations (e.g., Teng et al. 2009, Teng et al. 2015) are very useful to unambiguously detect hidden, even Compton-thick (with a hydrogen column density of $N_{\text{H}} > 10^{24} \text{ cm}^{-2}$) AGNs in ULIRGs thanks to their strong penetrating power, unless it largely exceeds $N_{\text{H}} \sim 10^{25} \text{ cm}^{-2}$.

UGC 5101 ($z = 0.040$), the subject of this paper, is a well-studied nearby ULIRG with an infrared (8–1000 μm) luminosity of $L_{\text{IR}} \simeq 10^{12} L_{\odot}$ (Table 1). It is optically classified as a LINER based on systematic investigation of luminous infrared galaxies (Veilleux et al. 1995), but there are some arguments that obscured AGN signatures (i.e., Seyfert 2) are detected in optical spec-

tra using some combination of optical emission lines (Goncalves et al. 1999; Yuan et al. 2010). Armus et al. (2004) detected high-excitation forbidden emission lines in the mid-infrared 5–30 μm , such as [Ne V] 14.3 μm and [O IV] 26 μm , which are naturally explained by the so-called narrow line regions (NLRs) photoionized by an AGN (Robson 1996). Signatures of an obscured AGN in UGC 5101 have been also seen in various methods, which do not rely on the emission from the NLRs, at the wavelengths of low dust extinction. A compact high surface-brightness emission was detected in the near-infrared 1–2 μm (Scoville et al. 2000) and mid-infrared 12.5 μm (Soifer et al. 2000), which may indicate the presence of a luminous AGN. Infrared 2.5–5 μm (Imanishi et al. 2001; Imanishi & Maloney 2003; Imanishi et al. 2008) and 5–35 μm (Armus et al. 2004; Nardini et al. 2009; Veilleux et al. 2009) spectral shapes, including the broad polycyclic aromatic hydrocarbon (PAH) emission features, are naturally explained by a luminous obscured AGN that contributes importantly to the observed flux at 2.5–35 μm . Millimeter interferometric observations using the Nobeyama Millimeter Array (NMA) showed an enhanced HCN J=1–0 to HCO⁺ J=1–0 emission-line flux ratio, compared to starburst-dominated galaxies (Imanishi et al. 2006), which is often seen in galaxies containing energetically important AGNs (Kohno 2005; Krips et al. 2008). Radio VLBI very high-spatial-resolution observations at 18 cm also sug-

TABLE 1
DETAILED INFORMATION OF UGC 5101

Object	Redshift	f_{12} [Jy] (3)	f_{25} [Jy] (4)	f_{60} [Jy] (5)	f_{100} [Jy] (6)	$\log L_{\text{IR}}$ ($\log L_{\text{IR}}/L_{\odot}$) [ergs s $^{-1}$] (7)
(1)	(2)	(3)	(4)	(5)	(6)	(7)
UGC 5101	0.040	0.25	1.03	11.54	20.23	45.5 (12.0)

NOTE. — (1) Object. (2) Redshift. (3)–(6) f_{12} , f_{25} , f_{60} , and f_{100} are the *IRAS FSC* fluxes at 12, 25, 60, and 100 μm , respectively. (7) Decimal logarithm of the infrared (8–1000 μm) luminosity in ergs s $^{-1}$ calculated as follows: $L_{\text{IR}} = 2.1 \times 10^{39} \times D(\text{Mpc})^2 \times (13.48 \times f_{12} + 5.16 \times f_{25} + 2.58 \times f_{60} + f_{100})$ ergs s $^{-1}$ (Sanders & Mirabel 1996). The values in parentheses are the decimal logarithms of the infrared luminosities in units of solar luminosities.

gest the presence of a luminous AGN (Smith et al. 1998; Lonsdale et al. 2003).

The AGN contribution to the bolometric luminosity in UGC 5101 is yet uncertain, however. According to Armus et al. (2007), the estimated AGN contribution based on the mid-infrared NLR-originated forbidden emission lines is less than 10%, which is substantially smaller than those by other energy diagnostic methods using mid-infrared continuum slope and equivalent width of the PAH emission features, > 50%. Because these mid-infrared lines emitted from the NLR are expected to be little affected by extinction, it is unlikely that weak NLR lines are attributed to dust absorption by interstellar gas in the host galaxy. Instead, a possible hypothesis is that the AGN in UGC 5101 is almost fully surrounded by dust located on inner scale with respect to the NLR, i.e., UGC 5101 contains a so called “buried AGN”. In a buried AGN, the NLR is under-developed compared to the majority of optical Seyfert galaxies because a large fraction of ionizing UV photons from the central AGN may be absorbed by dust at the very inner part before reaching the NLR. On the basis of 2–10 keV X-ray observations using *XMM-Newton* and *Chandra*, Imanishi et al. (2003) detected X-ray emission that is likely to originate in a Compton-thick AGN. They estimated the intrinsic (absorption-corrected) 2–10 keV luminosity to be $\approx 6 \times 10^{42}$ erg s $^{-1}$.¹ However, due to the limitation of the X-ray spectral coverage at <10 keV, large ambiguity remains about it. This source is also detected in the *Swift*/Burst Alert Telescope (BAT) 70-month survey covering the 14–195 keV band, and is listed as a Compton-thick AGN candidate (Ricci et al. 2015).

In this paper, we report the broadband X-ray spectra of UGC 5101 covering the 0.25–100 keV band, observed with *Swift*/BAT, *NuSTAR*, *Suzaku*, *XMM-Newton*, and *Chandra*. A combination of all available data provides us with an ideal opportunity to scrutinize the properties of such a Compton thick AGN in UGC 5101 in a much more reliable manner than in previous studies. We organize this paper as follows. Section 2 presents the details of the observations and reduction. Section 3 describes the results of spectral analysis. Section 4 discusses implications from our results. Section 5 states the conclusion of this paper. We adopt $H_0 = 70$ km s $^{-1}$ Mpc $^{-1}$, $\Omega_m = 0.27$, $\Omega_\lambda = 0.73$. The solar abundances by Anders & Grevesse

¹ This luminosity has been converted from the original value $\approx 5 \times 10^{42}$ erg s $^{-1}$ obtained for a Hubble constant of $H_0 = 75$ km s $^{-1}$ Mpc $^{-1}$ to that for $H_0 = 70$ km s $^{-1}$ Mpc $^{-1}$.

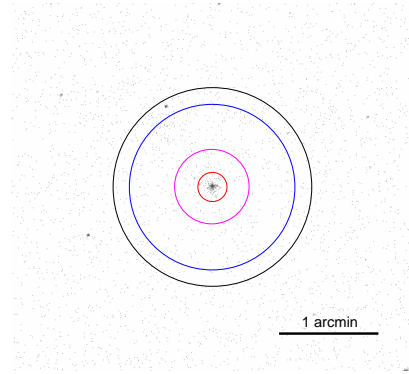


FIG. 1.— Spectral extraction regions marked on the *Chandra* image of UGC 5101 in the 0.3–7 keV band. The image size is 4 arcmin square. The red, magenta, blue, and black circular regions correspond to radii of 8.8 (*Chandra*), 22.5 (*XMM-Newton*), 50 (*NuSTAR*), and 60 arcsec (*Suzaku*), respectively.

(1989) and the photoelectric absorption cross-sections by Balucinska-Church & McCammon (1992) are assumed throughout this paper. All errors attached to spectral parameters correspond to 90% confidence limits for a single parameter of interest.

2. OBSERVATIONS AND DATA REDUCTION

We utilize the data observed with *NuSTAR*, *Suzaku*, *XMM-Newton*, and *Chandra*. To better constrain the broadband spectrum, we also use the time-averaged spectrum obtained in the *Swift*/BAT 70-month survey (<http://swift.gsfc.nasa.gov/results/bs70mon>). Table 2 lists the details of the observations. The spectral extraction regions and net count rate for each observatory are summarized in Table 3. These are chosen to maximize the signal-to-noise (S/N) ratio by considering the size of the point spread function, and to minimize the contamination from other sources. Figure 1 displays the *Chandra* image in the 0.3–7 keV band centered at UGC 5101 (see Section 2.4 for detail), where the source extraction regions are overlaid.

2.1. *NuSTAR*

The Nuclear Spectroscopic Telescope Array (*NuSTAR*) mission, launched on 2012 June 13, is the first focusing high-energy X-ray telescope, which covers the energy range of 3–78 keV (Harrison et al. 2013). It carries two co-aligned hard X-ray telescopes, each of which has its own focal plane module (FPMA and FPMB, FPMs). UGC 5101 was observed with *NuSTAR* on 2014 March 21 and 22 for a net exposure of 18.3 ksec. We reduce the data, using HEASoft version 6.17 and calibration

TABLE 2
SUMMARY OF OBSERVATIONS

	Instrument	Observation ID	Start Time* [UT]	End Time* [UT]	Exposure* [ks]
<i>Swift</i>	BAT	SWIFT J0935.9+6120	2004 December 16 00:00	2010 September 30 23:59	13428.3
<i>NuSTAR</i>	FPMA, FPMB	60001068002	2014 March 21 22:26	2014 March 22 09:01	18.3
<i>Suzaku</i>	XIS-0,1,2,3, HXD	701002010	2006 March 31 04:18	2006 April 1 08:25	49.0
		701002020	2006 October 31 18:19	2006 November 1 09:30	42.2
<i>XMM-Newton</i>	EPIC-MOS1,2, EPIC-pn	0085640201	2001 November 12 09:02	2001 November 12 18:35	33.9
<i>Chandra</i>	ACIS	2033	2001 May 28 07:02	2001 May 28 21:21	42.1

* Based on the information of FPMA for *NuSTAR*, XIS-0 for *Suzaku*, and EPIC-MOS1 for *XMM-Newton*.

TABLE 3
SUMMARY OF DATA REDUCTION

	Instrument	source radius [arcsec] (1)	background radius [arcsec] (2)	encircled energy fraction [%] (3)	net count rate [10^{-3} count s^{-1}] (4)
<i>Swift</i>	BAT	–	–	–	0.01
<i>NuSTAR</i>	FPMs	50	50	68	8.51
<i>Suzaku</i>	FI-XISs	60	100	~50	2.84
	BI-XIS	60	100	44	2.16
<i>XMM-Newton</i>	EPIC-MOSs	22.5	60	~80	6.94
	EPIC-pn	22.5	60	84	26.8
<i>Chandra</i>	ACIS	8.8	9.8–24.6	96	8.71

NOTE. — (1) The radius of the extraction region for the source spectrum. (2) The radius (or inner and outer radii) of the extraction region for the background spectrum. (3) The encircled energy fractions at 4.5 keV for *Suzaku*, at 6 keV for *XMM-Newton*, and at 6 keV for *Chandra*. (4) The net count rate after background subtraction.

database version 2015 September 4. We use the scripts *nupipeline* and *nuproducts* to make the spectra of FPMA and FPMB. Photon events in a circular region with a radius of 50 arcsec around the target are selected. The background spectrum is extracted from a nearby source-free circular region with the same size as the source region. We have verified that the FPMA and FPMB spectra give fully consistent results including the normalizations. Then, to improve the photon statistics in a single spectrum, the data of FPMA and FPMB are combined by using the script *addascaspec*.

Figure 2 plots the background-subtracted *NuSTAR* light curves in the 3–8 and 8–24 keV bands. The bin size is set to be 5760 sec (96 minutes), the orbital period of the satellite, to avoid any possible modulation related to orbital phase. The source and background regions are the same as those used for the spectral extraction. The FPMA and FPMB light curves are summed by using the *lcmath* task. Performing a χ^2 test to each light curve with a constant model, we find that time variability during the *NuSTAR* observation was not significant at $> 90\%$ confidence limits on timescales longer than 96 minutes in both energy bands.

2.2. *Suzaku*

Suzaku is the fifth observatory in a series of Japanese X-ray astronomy satellites (Mitsuda et al. 2007). It carries four X-ray CCD cameras called the X-ray Imaging Spectrometers (three Front-side-Illuminated XISs or FI-XISs, XIS-0, XIS-2, and XIS-3, and one Back-side-Illuminated XIS or BI-XIS, XIS-1, Koyama et al. 2007) and a non-imaging instrument that consist of Si PIN photo-diodes and Gadolinium Silicon Oxide (GSO) scintillation counters, called the Hard X-ray Detector (HXD,

Takahashi et al. 2007). UGC 5101 was observed with *Suzaku* on 2006 March 31, April 1 and 2006 October 31, November 1 for exposures of 49.0 ksec and 42.2 ksec, respectively. We analyze the data in a standard manner, using HEASoft version 6.17 and calibration database released on 2015 October 5.

2.2.1. XIS

The XISs cover the energy range below ≈ 10 keV. To extract the spectra, we accumulate photon events in the circle centered at the source with a radius of 60 arcsec. The background is taken from a source-free region in the field of view. In the source extraction region, the *Chandra* image (Figure 1) shows another, much fainter point-like source, whose distance from the target is ~ 55 arcsec, and therefore we add its estimated contribution to the background by analyzing the *Chandra* data. We confirm that the contribution of this source is negligible in the spectra of the other instruments, including *NuSTAR*/FPMs.

We sum up the spectra of XIS-0, XIS-2 and XIS-3, whereas the XIS-1 spectrum was treated independently. Since no significant variability in the spectra was found between the two observation epochs, we make the time averaged spectra by combining them.

2.2.2. HXD

We also examine the data of HXD/PIN, which covers the energy range of 14–70 keV and hence are suitable for detecting the transmitted component from a Compton-thick AGN. The “tuned” background file (version 2.0) released from the *Suzaku* team is used as the non Xray background (NXB), while the Cosmic X-ray Background (CXB) is estimated by assuming the spectral form presented in Boldt (1987).

The response files `ae_hxd_pinhxnome3_20080129.rsp` and `ae_hxd_pinflate3_20080129.rsp` are used to estimate the source flux and the CXB, respectively.

No significant signals from UGC 5101 are detected with HXD/PIN. The count rate in the 15–40 keV after subtraction of the NXB and CXB is $0.00085 \text{ counts s}^{-1}$, which is 0.30% of that of the NXB. The 3σ upper limit on the count rates is $0.0085 \text{ counts s}^{-1}$, which is 3% of the NXB rate (Fukazawa et al. 2009). This upper limit corresponds to a hard X-ray flux of $3.8 \times 10^{-12} \text{ erg cm}^{-2} \text{ s}^{-1}$ in the 15–40 keV band for Model Ib (see Section 3.1.2), which is 1.8 and 1.2 times larger than the actual fluxes measured with *Swift*/BAT and *NuSTAR*, respectively.

2.3. XMM-Newton

We analyze the *XMM-Newton* EPIC data obtained on 2001 November 12. To take into account the latest calibration, the data are reprocessed and analyzed by using the Science Analysis System (SAS) version 14.0.0 and the latest calibration files (CCF) as of 2015 October. We examine light curves of PATTERN=0 events in the energy range of 10–12 keV (for EPIC-pn) or above 10 keV (for EPIC-MOS), and find that the background fluxes are relatively stable, although some flux increases during the observation are seen. We apply no filter to discard such time intervals. The source and background spectra are extracted from a circular region with a radius of 22.5 arcsec and a source free region in the same CCD chip, respectively. Only PATTERN ≤ 4 and PATTERN ≤ 12 events are used for EPIC-pn and EPIC-MOS, respectively. The redistribution matrix function (RMF) and auxiliary response file (ARF) are made using the SAS tasks `rmfgen` and `arfgen`.

2.4. Chandra

A *Chandra* observation of UGC 5101 was performed on 2001 May 28. The ACIS was operated in the FAINT mode. The *Chandra* data are reprocessed and analyzed using the *Chandra* Interactive Analysis of Observations (CIAO) software package version 4.7 combined with the calibration CALDB version 4.6.9. UGC 5101 is located in the ACIS-S3 back-illuminated CCD chip. The data are screened by applying the `lc_clean` script for the light curve in the 0.5–7 keV band of the whole ACIS-S3 excluding bright sources. Only the events with grade 0, 2, 3, 4, 6 are used in the following analysis. The source spectrum is extracted from a circular region with a radius of 8.8 arcsec centered at the position of UGC 5101. We find from the 0.3–7 keV image (Figure 1) that there is diffuse emission extending ~ 18 arcsec in the north-south direction and ~ 8 arcsec in the east-west direction around the point-like source. Most of these photon counts are also included in the spectral extraction region. The background spectrum is taken from an annular region around the source. The spectra, RMF and ARF are created by using the script `specextract` in the CIAO package. Benefiting from its unsurpassed high image quality (full width at half maximum ~ 0.5 arcsec), *Chandra* data are suitable for studying possible contamination from other sources (see Section 2.2.1).

3. SPECTRAL ANALYSIS

We simultaneously analyze the set of seven spectra (*Swift*/BAT, *NuSTAR*/FPMs, *Suzaku*/FI-XISs and

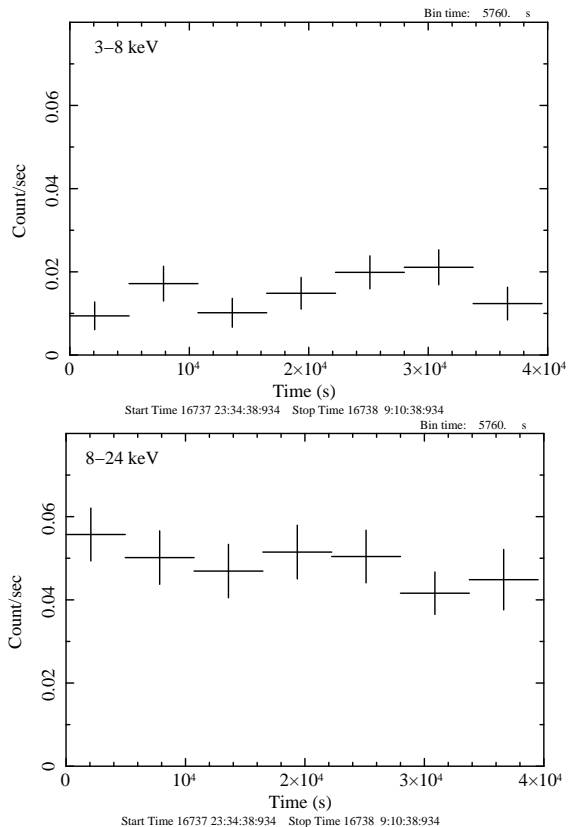


FIG. 2.— *NuSTAR* light curves in the 3–8 keV and 8–24 keV bands. The bin size is 5760 sec.

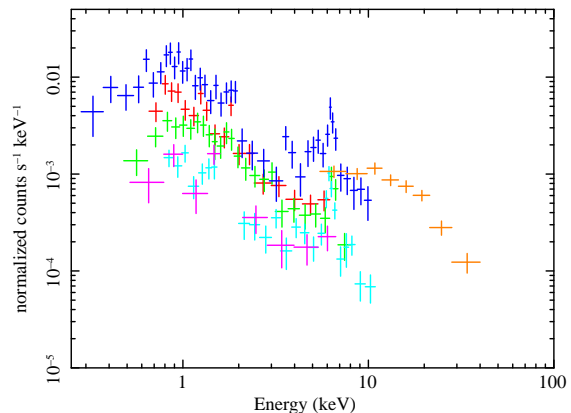


FIG. 3.— Observed spectra of UGC 5101 folded with the energy responses. The orange, light blue, magenta, green, blue and red crosses represent the data of FPMs, FI-XISs, BI-XIS, EPIC-MOS, EPIC-pn, and ACIS, respectively.

BI-XIS, *XMM-Newton*/EPIC-pn and EPIC-MOSs, and *Chandra*/ACIS). Figure 3 shows the observed spectra folded with the energy responses except for *Swift*/BAT. A prominent Fe $K\alpha$ line at 6.4 keV can be clearly seen in Figure 3.

For spectral analysis, we use the data of BAT, FPMs, FI-XISs, BI-XIS, MOSs, pn, and ACIS in the energy bands of 14–100 keV, 5.5–40 keV, 0.8–11 keV, 0.5–7 keV, 0.5–8 keV, 0.25–10 keV, and 0.65–6 keV, respectively, where the signal-to-noise ratio is sufficiently high. The data of FI-XISs and BI-XIS in the 1.6–1.9 keV band are

excluded to avoid calibration uncertainties. The spectral bins are merged to contain at least 100, 50, 20, and 20 counts for each spectrum of *NuSTAR*, *Suzaku*, *XMM-Newton*, and *Chandra*, respectively. Spectral fit is performed on XSPEC with the χ^2 minimization method. To take into account the Galactic absorption, **phabs** is always multiplied to the spectral model, whose hydrogen column density is fixed at the value based on the H_I map (Kalberla et al. 2005). We multiply a constant factor (**const0**; N_{FI} , N_{BI} , N_{MOS} , N_{pn} , and N_{ACIS} for FI-XISs, BI-XIS, EPIC-MOSs, EPIC-pn, and ACIS, respectively) to each spectrum in order to correct for cross calibration uncertainties in the absolute flux among different instruments. It is fixed at unity for the BAT spectrum, which is adopted as calibration references in this paper. For the other instruments, it is allowed to vary within a reasonable range, 0.8–1.2. Furthermore, we link the **const0** factor of FPMs to those of MOSs because their relative normalizations are well calibrated within a few percents (Madsen et al. 2015); we confirm that these few percent uncertainties have negligible effects on the spectral parameters. In addition, we also consider possible time variability of the AGN emission (see below) with respect to the averaged flux measured with *Swift*/BAT over 70 months.

3.1. Analytical Models

3.1.1. Model Ia

First we start with Model B in Imanishi et al. (2003) adopted to fit the *XMM-Newton* and *Chandra* spectra. The model consists of a primary, heavily absorbed power law with an exponential cutoff (hereafter “cutoff power law”), a less absorbed cutoff power law (or a scattered component), a narrow gaussian representing an iron-K emission line, and an optically-thin thermal component. In XSPEC, this model (hereafter “Model Ia”) is described as:

$$\begin{aligned} & \text{const0} * \text{phabs} * \{ \text{zphabs1} \\ & * (\text{const1} * \text{zphabs2} * \text{zpowerlw} * \text{zhighect} \\ & + \text{const1} * \text{zgauss} \\ & + \text{const2} * \text{zpowerlw} * \text{zhighect}) \\ & + \text{apec}. \} \end{aligned} \quad (1)$$

We fix a cutoff energy² at 360 keV, the value adopted in the torus model by Ikeda et al. (2009) (Model II, see Section 3.2), because it cannot be well constrained from the data; variation of the cutoff energy within a reasonable range (100–500 keV) has little influence on the spectral parameters in Models Ia and Ib (Section 3.1.2). The constant factor **const1** is introduced to account for possible time variability of the AGN component relative to the flux measured with *Swift*/BAT. Except for *NuSTAR*, it is found to be consistent with unity within the expected instrumental cross normalizations (**const0**). Hence, it is left free for the *NuSTAR* spectrum (N_{FPM}^{time}) and is fixed at unity for the other spectra in the final spectral fit. The **const2** factor gives the scattering fraction, f_{scat} . We define it as the ratio of the unabsorbed fluxes at 1

keV between the scattered and primary power law components, whose normalizations are tied together. The photon index of the scattered component is set to be independent of that of the primary one. The weak absorption (**zphabs1**, $N_H^{\text{host}} \sim 1 \times 10^{21} \text{ cm}^{-2}$) to the second power-law component is significantly required from the data, although this fact was (mistakenly) not mentioned in Imanishi et al. (2003); otherwise, the model leaves large negative residuals below ~ 1 keV. We confirm that the presence of this absorption is robust against modelling of the scattered component in both Models Ia and Ib; it is still required when we include emission lines and radiative recombination continua of a photoionized plasma whose flux ratios are fixed to those in NGC 1068 (Guainazzi & Bianchi 2007), and when the photon index is tied to that of the primary component.

This phenomenological model gives an acceptable fit of our combined spectra ($\chi^2/\text{d.o.f.} = 123.40/117$). Table 4 lists the best fit parameters, the observed fluxes and intrinsic (de-absorbed) luminosities in the 2–10 keV and 10–50 keV bands, and the equivalent width of the iron-K line with respect to the total continuum. The fluxes and luminosities are based on the *Swift*/BAT spectrum, for which **const0** and **const1** are set unity. Figure 4 and Figure 5 present the unfolded spectra and best-fit models for Model Ia, respectively. The line center energy becomes 6.46 keV. It is consistent with a fluorescence line from cold matter as the main component, although weak contribution from ionized lines (e.g., Iwasawa et al. 2011) is possible.

3.1.2. Model Ib

Next, we consider a more physically motivated model than Model Ia. Firstly, a Compton reflection continuum from the torus should be present, which accounts for the origin of the narrow iron-K α line. Secondly, in the case of a Compton-thick torus, we should take into account Compton scattering for the transmitted component in addition to photoelectric absorption. Assuming an extreme case where the absorber is located only along the line of sight (i.e., photons scattering into the line of sight from other directions are ignorable), this can be modelled by multiplying **cabs** to the transmitted component. We thus adopt the following analytical model as our “Model Ib”. Similar spectra are often observed from ULIRGs (e.g., Teng et al. 2015). This model is expressed in the XSPEC terminology as:

$$\begin{aligned} & \text{const0} * \text{phabs} * \{ \text{zphabs1} \\ & * (\text{const1} * \text{zphabs2} * \text{cabs} * \text{zpowerlw} * \text{zhighect} \\ & + \text{const1} * \text{pexmon} \\ & + \text{const2} * \text{zpowerlw} * \text{zhighect}) \\ & + \text{apec}. \} \end{aligned} \quad (2)$$

(1) The first term represents the transmitted component from the AGN, modelled by an absorbed cutoff power law with a cutoff energy of 360 keV. The **const1** factor, which accounts for time variation with respect to the *Swift*/BAT spectrum, is linked to that for the reflection (second) component. (2) The second term approximately describes a reflection component from the torus. Here we utilize the **pexmon** code (Nandra et al. 2007). This combines the **pexrav** model, which calculates a Compton-reflection continuum from optically

² This corresponds to an e-folding energy (E_f) in the **zhighect** model when E_c is set to be zero.

thick, cold matter (Magdziarz & Zdziarski 1995), with fluorescence lines from heavy elements. The relative intensity is defined as $R \equiv \Omega/2\pi$, where Ω is the solid angle of the reflector. We leave R free within a range of $-2 \leq R < 0$ and fix the inclination angle at 60 degree as a representative value for a geometrically thick torus (e.g., Eguchi et al. 2009; Kawamuro et al. 2016). The negative values of R indicate that the **pexmon** model represents only the reflection component. The photon index, cut-off energy, and normalization are linked to those of the transmitted component. We do not apply absorption to the reflection component, which is not significantly ($>90\%$ confidence level) required from the data. The same constant factor **const1** as the first term is multiplied to the second term in order to take into account time variability, although this assumption may not be trivial, depending on the location of the reflector.³ (3) The third term is the scattered component of the intrinsic AGN spectrum, modelled with a cutoff power-law whose parameters except photon index are linked to those in the transmitted component, multiplied by **const2** (f_{scat}). A weak absorption (**zphabs1**) is multiplied to the first, second and third terms. We assume that the third and fourth components did not vary among the multiple observation epochs, considering the large spatial scales of the emitting regions. (4) The fourth term accounts for optically-thin thermal emission in the host galaxy. Here we ignore any intrinsic absorption.

We find that this model also well reproduces the combined spectra covering the 0.25–100 keV band ($\chi^2/\text{d.o.f} = 130.59/118$). Table 4 lists the best-fit parameters, the observed fluxes and intrinsic luminosities in the 2–10 keV and 10–50 keV bands based on the *Swift*/BAT spectrum, and the 6.4 keV line equivalent-width predicted from the best-fit model. The unfolded spectra and best-fit models are presented in Figures 4 and 5, respectively. The line-of-sight column density of the transmitted component is found to be $N_{\text{H}}^{\text{LS}} = 1.26_{-0.31}^{+0.33} \times 10^{24} \text{ cm}^{-2}$, which identifies UGC 5101 as a Compton-thick AGN, consistent with the result of Model Ia.

3.2. Torus Model

As an even more realistic picture, we utilize the torus model by Ikeda et al. (2009) (hereafter “Ikeda torus model”), a numerical spectral model based on Monte Carlo simulations. The Ikeda torus model assumes a nearly spherical torus consisting of neutral, cold material and has two cone-shaped holes along the polar axis. The geometry is determined by the torus half-opening angle (θ_{op} within a range of 0–70 degree), inclination angle (θ_{incl} within a range of 1–89 degree), and the ratio of the inner to outer radii, $r_{\text{in}}/r_{\text{out}}$, which is fixed at 0.01. The variable half-opening angle is one of the advantages of this model among similar numerical models, because it is expected not to be constant in AGNs. The incident spectrum is a cutoff power law with a cutoff energy of 360 keV. The other free parameters of this model are photon index (Γ_{AGN}) and column density along the equatorial plane (N_{H}^{Eq}), which are variable between 1.5–2.5 and between 10^{22} – 10^{25} cm^{-2} , respectively (see Ikeda et al. 2009

³ We obtain $R = -0.11_{-0.19}^{+0.07}$ when the **const1** factor is not multiplied to the **pexmon** component. Thus, the conclusion of small R is unchanged.

for details). We fix the inclination angle at 80 degrees, in order to assure a type-2 AGN geometry, while the half opening angle is left free. The equatorial column density, photon index, and normalization are linked to those of the transmitted component.

In the XSPEC terminology, the total model (Model II) is represented as follows:

$$\begin{aligned} & \text{const0} * \text{phabs} * \{ \text{zphabs1} \\ & * (\text{const1} * \text{torusabs} * \text{zpowerlw} * \text{zhightect} \\ & + \text{const1} * \text{atable}\{\text{refl1_torus.fits}\} \\ & + \text{const1} * \text{atable}\{\text{refl2_torus.fits}\} \\ & + \text{const1} * \text{atable}\{\text{refl_fe_torus.fits}\} \\ & + \text{const2} * \text{zpowerlw} * \text{zhightect} \\ & + \text{apec} \} \end{aligned} \quad (3)$$

The model consists of six components: (1) the transmitted component from the AGN, (2) the torus reflection component absorbed by the near-side torus, (3) that not absorbed by the near-side torus, (4) the iron-K α emission line, (5) the scattered component (with a photon index Γ_{scat} and a scattering fraction of f_{scat}), and (6) the optically-thin thermal component. Similarly to the case of analytical models, we consider time variability of the (1)-(4) components for the *NuSTAR* data. We do not utilize the energy band below 0.7 keV with Model II, where the Ikeda torus model is not available. Hence, the absorption from the host galaxy and the parameters of the optically-thin thermal component are fixed at the same values as in Model Ib, which cannot be well constrained with the data above 0.7 keV. We confirm that changing the fixed parameters within the uncertainties does not affect the conclusions.

This model also well reproduces the combined spectra of UGC 5101 in the 0.7–100 keV band ($\chi^2/\text{d.o.f} = 126.22/111$). Table 5 lists the best-fit parameters, the observed fluxes and intrinsic luminosities in the 2–10 keV and 10–50 keV bands based on the *Swift*/BAT spectrum, and the iron-K line equivalent width with respect to the total continuum. The unfolded spectra and best-fit model are plotted in Figures 4 and 5, respectively. The line-of-sight column density calculated from the equation (3) in Ikeda et al. (2009) becomes $N_{\text{H}}^{\text{LS}} = 1.31_{-0.36}^{+0.31} \times 10^{24} \text{ cm}^{-2}$, confirming that the galaxy contains a Compton thick AGN. The data prefer a large half-opening angle, $\theta_{\text{op}} > 41$ degrees, with the best-fit of 70 degrees (the maximum value in the table model). With this geometry ($\theta_{\text{op}} = 70$ and $\theta_{\text{inc}} = 80$), the fraction of the reflection component from the far-side torus absorbed (unabsorbed) by the near-side torus is $\approx 7\%$ ($\approx 93\%$). We find that the 10–50 keV intrinsic luminosity would be reduced by $\sim 6\%$ from our best estimate within the uncertainty in the torus opening angle (41–70 degrees). This uncertainty does not affect our conclusions.

4. DISCUSSION

We have presented the first high-quality broadband X-ray spectra of UGC 5101 in the 0.25–100 keV band, observed with *Swift*, *NuSTAR*, *Suzaku*, *XMM-Newton*, and *Chandra*. The combined data, whose total exposure except *Swift*/BAT is 185.5 ksec, have enabled us to best constrain the spectral properties of this target. Besides the AGN contribution, we confirm the presence of

TABLE 4
BEST FIT PARAMETERS OF ANALYTICAL MODELS

Note*	Parameter	Model Ia	Model Ib
(1)	$N_{\text{H}}^{\text{host}} [10^{21} \text{ cm}^{-2}]$	$1.06^{+0.80}_{-0.60}$	$1.46^{+0.88}_{-0.66}$
(2)	$N_{\text{H}}^{\text{LS}} [10^{24} \text{ cm}^{-2}]$	$1.11^{+0.21}_{-0.27}$	$1.26^{+0.33}_{-0.31}$
(3)	Γ_{AGN}	$1.40^{+0.36}_{-0.30}$	$1.61^{+0.34}_{-0.31}$
(4)	$A_{\text{AGN}} [10^{-3} \text{ keV}^{-1} \text{ cm}^{-2} \text{ s}^{-1}]$	$0.23^{+0.55}_{-0.16}$	$1.0^{+3.3}_{-0.8}$
(5)	R	–	$-0.10^{+0.06}_{-0.15}$
(6)	$E_{\text{cent}} [\text{keV}]$	6.46 ± 0.04	–
(7)	$A_{\text{iron}} [10^{-6} \text{ cm}^{-2} \text{ s}^{-1}]$	$1.20^{+0.44}_{-0.43}$	–
(8)	$f_{\text{scat}} [\%]$	6^{+12}_{-4}	$1.4^{+4.5}_{-1.1}$
(9)	Γ_{scat}	$1.47^{+0.23}_{-0.21}$	$1.74^{+0.27}_{-0.25}$
(10)	$kT [\text{keV}]$	0.90 ± 0.12	$0.88^{+0.13}_{-0.12}$
(11)	$A_{\text{apex}} [10^{-6} \text{ cm}^{-5}]$	$2.2^{+0.9}_{-0.8}$	$2.0^{+0.9}_{-0.8}$
(12)	N_{FI}	$1.06^{+0.14}_{-0.13}$	1.07 ± 0.13
(13)	N_{BI}	$1.04^{+0.18}_{-0.21}$	$1.05^{+0.15}_{-0.21}$
(14)	N_{MOS}	$0.92^{+0.19}_{-0.11}$	$0.92^{+0.18}_{-0.11}$
(15)	N_{pn}	$0.93^{+0.19}_{-0.10}$	$0.94^{+0.18}_{-0.10}$
(16)	N_{ACIS}	$0.80 (< 0.96)$	$0.80 (< 0.95)$
(17)	$N_{\text{FPM}}^{\text{time}}$	$1.69^{+0.45}_{-0.35}$	$1.63^{+0.42}_{-0.32}$
(18)	$F_{2-10} [\text{erg cm}^{-2} \text{ s}^{-1}]$	1.9×10^{-13}	1.9×10^{-13}
(19)	$F_{10-50} [\text{erg cm}^{-2} \text{ s}^{-1}]$	3.2×10^{-12}	3.2×10^{-12}
(20)	$L_{2-10} [\text{erg s}^{-1}]$	5.1×10^{42}	1.6×10^{43}
(21)	$L_{10-50} [\text{erg s}^{-1}]$	1.2×10^{43}	2.9×10^{43}
(22)	$\text{EW} [\text{eV}]$	361 (1433)	202 (1433)
	χ^2/dof	123.40 / 117	130.59 / 118

* (1) The hydrogen column density for all AGN components. (2) The hydrogen column density for the AGN transmitted component. (3) The power-law photon index of the AGN transmitted component. (4) The power-law normalization of the AGN transmitted component at 1 keV. (5) The relative reflection intensity. (6) The central energy of the iron-K α emission line. (7) The normalization of the iron-K α emission line. (8) The scattering fraction. (9) The power-law photon index of the scattered component. (10) The temperature of the thermal component. (11) The normalization of the thermal component. (12) The cross normalization of FI-XISs relative to BAT. (13) The cross normalization of BI-XIS relative to BAT. (14) The cross normalization of EPIC-MOSs relative to BAT. (15) The cross normalization of EPIC-pn relative to BAT. (16) The cross normalization of ACIS relative to BAT. (17) The time variability normalization of FPMs relative to BAT. (18) The observed flux in the 2–10 keV band. (19) The observed flux in the 10–50 keV band. (20) The de-absorbed AGN luminosity in the 2–10 keV band. (21) The de-absorbed AGN luminosity in the 10–50 keV band. (22) The equivalent width of the iron-K emission line with respect to the total continuum (the reflection continuum).

optically-thin thermal emission at low energies ($< 2\text{keV}$) as previously reported by Imanishi et al. (2003). The temperature ($\approx 0.88 \text{ keV}$) and luminosity ($\approx 1.1 \times 10^{39} \text{ erg s}^{-1}$ in the 2–10 keV band) of the thin thermal component, which is spatially resolved in the *Chandra* image (Imanishi et al. 2003), is typical of ULIRGs (e.g., Iwasawa et al. 2011).

As for the AGN contribution, we have shown that two analytical models (Models Ia and Ib) and Monte-Carlo based numerical torus model (Model II) can well reproduce the data in terms of χ^2 test. Model Ia is a simple, phenomenological model, while Model Ib is a more physically motivated model including a reflection component from Compton-thick matter. In Model II, a more realistic geometry of the torus is considered. With our analysis, we firmly confirm the presence of a luminous Compton-thick AGN in UGC 5101, whose transmitted component is detected in the hard X-ray band above 10 keV. The basic spectral parameters (photon index and absorption) are consistent within their uncertainties among the three models. We note, however, that if the Compton reflection component, required by the data, is not considered in the model, a slightly flatter intrinsic photon index is derived for the primary power-law component, i.e., $\Gamma_{\text{AGN}} \approx 1.4$ (Model Ia) to be compared with $\Gamma_{\text{AGN}} \approx 1.6$ (Model Ib and Model II). More importantly,

we find that if Compton scattering of the transmitted component is ignored (Model Ia), the intrinsic X-ray luminosity is significantly underestimated compared with Model II: a factor ~ 2 in the 10–50 keV band and a factor ~ 3 in the 2–10 keV band (see Tables 4 and 5). The Model Ia result is very similar to the previous estimate by Imanishi et al. (2003) ($\approx 6 \times 10^{42} \text{ erg s}^{-1}$), in which the Compton scattering effects were also ignored. By contrast, in Model Ib, we apply the **cabs** model to the transmitted component, assuming an extreme geometry where the absorber is located only in the line of sight (see Section 3.1.2). In this case, the luminosities are slightly overestimated compared with Model II. Hereafter, we refer to the luminosities obtained with Model II unless otherwise stated, because we consider it the most physically self-consistent model among the three. We note that all luminosities listed in Table 4 and 5 are based on the *Swift*/BAT spectrum, because we are interested in time averaged values when discussing the spectral energy distribution. Even if we adopt the luminosity obtained with *NuSTAR*, which is higher than the *Swift*/BAT one by a factor of $1.54^{+0.36}_{-0.29}$, our main conclusions are unaffected.

The fitting result with the torus model of Ikeda et al. (2009), $\theta_{\text{op}} > 41$ degrees, suggests that the covering fraction of Compton-thick parts of the torus is only moderate. This result is consistent with the best-fit

TABLE 5
BEST FIT PARAMETERS OF MODEL II

Note*	Parameter	
(1)	$N_{\text{H}}^{\text{host}}$ [10^{21} cm $^{-2}$]	1.46 †
(2)	N_{H}^{Eq} [10^{24} cm $^{-2}$]	1.32 $^{+0.32}_{-0.37}$
(3)	θ_{op} [degree]	70 (> 41)
(4)	Γ_{AGN}	1.63 $^{+0.27}_{-0.13}$
(5)	A_{AGN} [10^{-3} keV $^{-1}$ cm $^{-2}$ s $^{-1}$]	0.9 $^{+2.0}_{-0.5}$
(6)	f_{scat} [%]	1.5 $^{+1.5}_{-1.0}$
(7)	Γ_{scat}	1.58 $^{+0.13}_{-0.14}$
(8)	kT [keV]	0.88 †
(9)	A_{apec} [10^{-6} cm $^{-5}$]	2.0 †
(10)	N_{FI}	1.07 $^{+0.13}_{-0.13}$
(11)	N_{BI}	1.04 $^{+0.16}_{-0.22}$
(12)	N_{MOS}	0.92 $^{+0.27}_{-0.11}$
(13)	N_{pn}	0.93 $^{+0.21}_{-0.10}$
(14)	N_{ACIS}	0.80 (< 1.0)
(15)	$N_{\text{FPM}}^{\text{time}}$	1.54 $^{+0.36}_{-0.29}$
(16)	F_{2-10} [erg cm $^{-2}$ s $^{-1}$]	2.0×10^{-13}
(17)	F_{10-50} [erg cm $^{-2}$ s $^{-1}$]	3.3×10^{-12}
(18)	L_{2-10} [erg s $^{-1}$]	1.4×10^{43}
(19)	L_{10-50} [erg s $^{-1}$]	2.4×10^{43}
(20)	EW [eV]	245
	χ^2/dof	126.22 / 111

* (1) The hydrogen column density for all AGN components. (2) The hydrogen column density for the AGN transmitted component. (3) The half opening angle of the torus. (4) The power-law photon index of the AGN transmitted component. (5) The power-law normalization of the AGN transmitted component at 1 keV. (6) The scattering fraction. (7) The power-law photon index of the scattered component. (8) The temperature of the thermal component. (9) The normalization of the thermal component. (10) The cross normalization of FI-XISs relative to BAT. (11) The cross normalization of BI-XIS relative to BAT. (12) The cross normalization of EPIC-MOSs relative to BAT. (13) The cross normalization of EPIC-pn relative to BAT. (14) The cross normalization of ACIS relative to BAT. (15) The time variability normalization of FPMs relative to BAT. (16) The observed flux in the 2–10 keV band. (17) The observed flux in the 10–50 keV band. (18) The de-absorbed AGN luminosity in the 2–10 keV band. (19) The de-absorbed AGN luminosity in the 10–50 keV band. (20) The equivalent width of the iron-K emission line with respect to the total continuum.

† fixed at the same values as in Model Ib.

scattering fraction, $f_{\text{scat}} \sim 1.5\%$, which implies that UGC 5101 is not a “low scattering fraction AGN” with $f_{\text{scat}} < 0.5\%$, putative population of AGNs with small torus opening angles discovered by hard X-ray surveys (Ueda et al. 2007). The scattering fraction of UGC 5101 is similar to, and even larger than, the median values of an [O III] $\lambda 5007$ selected sample ($f_{\text{scat}} \sim 1.5\%$; Noguchi et al. 2010) and a hard X-ray (14–195 keV) selected sample ($f_{\text{scat}} \sim 1\%$; Kawamuro et al. 2016), respectively. We note, however, that given the large error in the scattering fraction and possible contamination by emission from high mass X-ray binaries in the host galaxy, we cannot make strong arguments based on the f_{scat} value.

These results imply that the nucleus in UGC 5101 cannot be fully surrounded by Compton-thick matter. Nevertheless, there could be the possibility that a lower column-density (Compton-thin) absorber is present in the torus-hole regions that attenuates the nuclear ionizing UV emission and causing the under-developed NLR in UGC 5101 (Section 1). By our analysis, we indeed

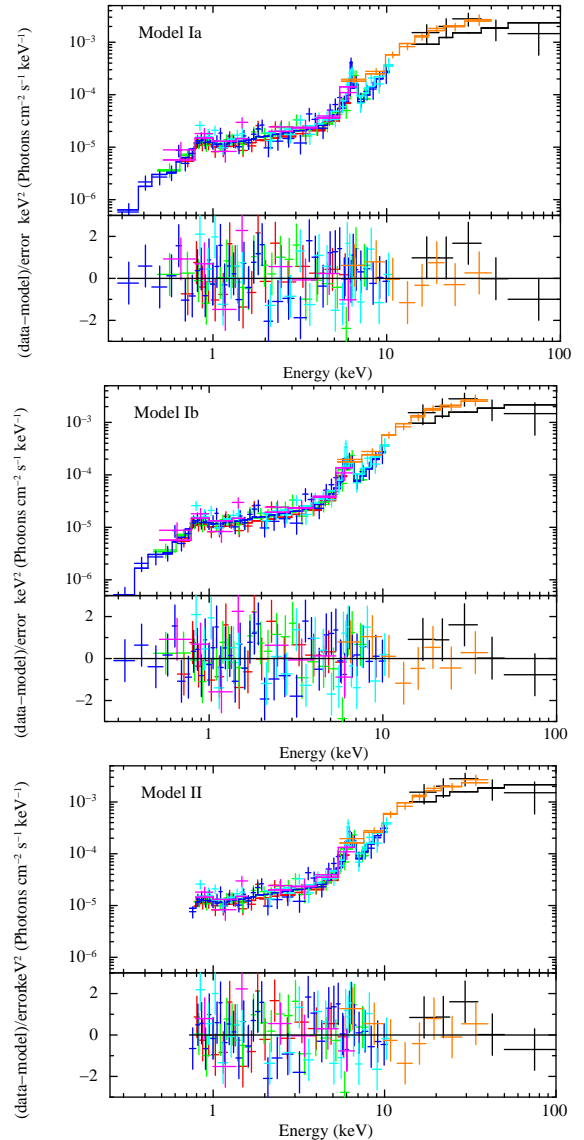


FIG. 4.— Unfolded spectra for Model Ia, Model Ib, and Model II. The black, orange, light blue, magenta, green, blue, and red crosses are the data of BAT, FPMs, FI-XISs, BI-XIS, EPIC-MOS, EPIC-pn, and ACIS, respectively. The solid lines represent the best-fit models.

find that a weak intrinsic X-ray absorption ($N_{\text{H}}^{\text{host}} \sim 10^{21}$ cm $^{-2}$, **zphabs1** in Section 3), in addition to the Compton-thick absorber, is required when the data below 0.7 keV, which are sensitive to determine such an absorption, are included in the fit (i.e., Models Ia and Ib). By assuming a Galactic dust-to-gas ratio, this column density corresponds to an optical extinction of $A_V \sim 0.5$ mag (Güver & Özel 2009). This is sufficient to block a large fraction of ionizing UV lights from the central engine of the AGN, although we cannot discard the possibility that the absorption could be associated to interstellar medium of the host galaxy on a larger scale.

To further investigate the nuclear geometry and intrinsic spectral energy distribution, we compare the luminosity of an emission line from the NLR and the AGN X-ray luminosity. Figure 6 plots the correlation between the [O IV] 26 μm luminosity and the absorption-corrected

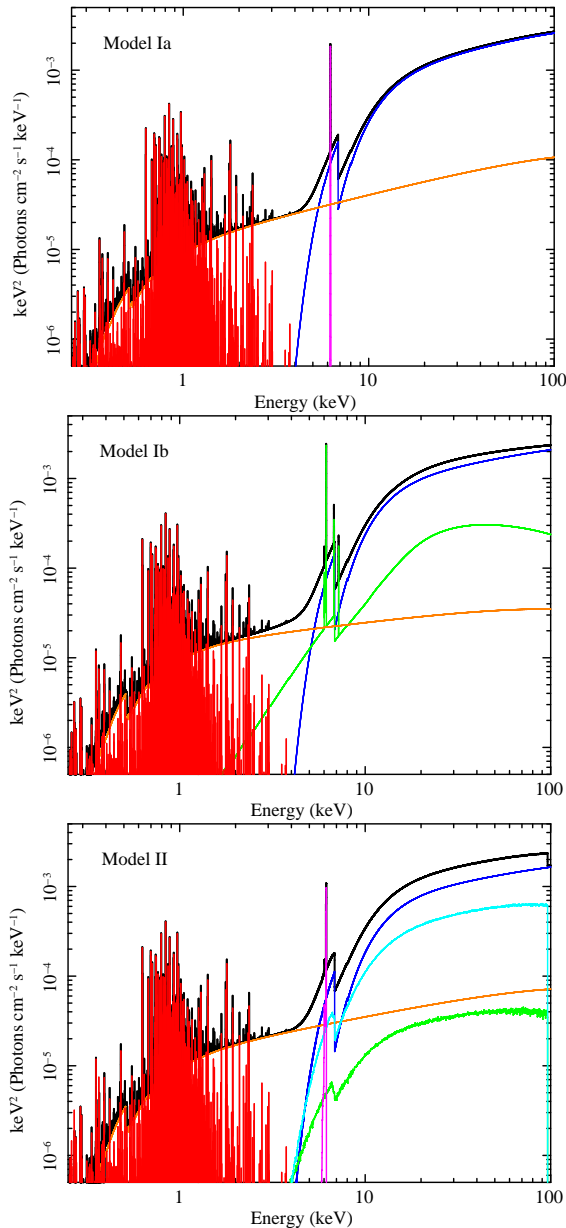


FIG. 5.— Best-fit models for Model Ia, Model Ib, and Model II. For Model Ia, the black, blue, orange, magenta, and red lines represent the total, directly transmitted component, scattered component, iron-K α emission line, and thermal emission, respectively. For Model Ib, the black, blue, orange, green, and red lines represent the total, directly transmitted component, scattered component, reflection component by *pexmon*, and thermal emission, respectively. For Model II, the black, blue, orange, green, light blue, magenta, and red lines represent the total, directly transmitted component, scattered component, absorbed reflection component, unabsorbed reflection component, iron-K α emission line, and thermal emission, respectively.

2–10 keV AGN luminosity for UGC 5101 (square). Assuming that the ratio between the [O IV] 26 μm and far-infrared (FIR) luminosity in pure starburst galaxies is typically $L_{[\text{O IV}]} / L_{\text{FIR}} \sim 10^{-5}$ (e.g., see Figure 22 of Veilleux et al. 2009), we estimate that starburst contamination in the observed [O IV] 26 μm luminosity is very small, $\sim (1 - f_{\text{AGN}}) \times 10\%$, where f_{AGN} is the fractional AGN contribution to the total bolomet-

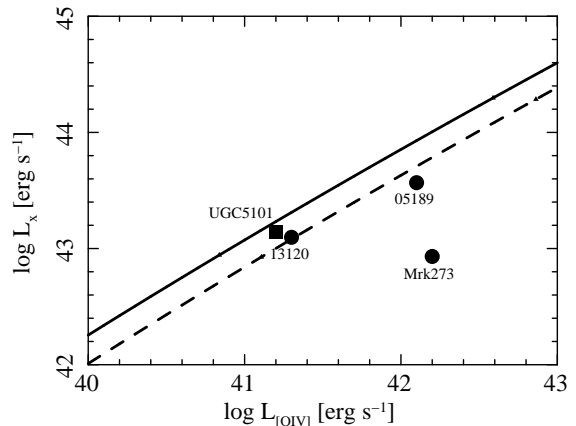


FIG. 6.— Comparison between the absorption-corrected 2–10 keV AGN luminosity and the [O IV] 26 μm luminosity for UGC 5101 (square) and typical ULIRGs observed by Teng et al. (2015) (IRAS 05189–2524, IRAS 13120–5453, and Mrk 273, circles). The solid and dashed lines represent the expected relations based on Rigby et al. (2009) for Seyfert 1 and Compton-thin Seyfert 2 galaxies, respectively.

ric luminosity (see below). The flux ratio between [Ne V] 14.3 μm and [O IV] 26 μm lines also supports that the [O IV] luminosity is dominated by the AGN component (Armus et al. 2007). For comparison, we also plot the data of other ULIRGs, IRAS 05189–2524, IRAS 13120–5453, and Mrk 273, taken from the sample observed by Teng et al. (2015) by excluding Superantenna (IRAS F19254–7245), a candidate of a heavily Compton thick AGN ($N_{\text{H}}^{\text{LS}} > 10^{25} \text{ cm}^{-2}$), and Mrk 231, a probable outlier object (broad absorption line QSO). The curves represent the expected relations for Seyfert 1 (solid) and Compton-thin Seyfert 2 galaxies (dashed) based on the average $L_{\text{bol}} / L_{[\text{O IV}]}$ ratio obtained by Rigby et al. (2009) with the 2–10 keV to bolometric luminosity conversion factor given by Marconi et al. (2004).

As noticed from Figure 6, the [O IV] to X-ray luminosity ratio in UGC 5101 is similar to those of normal Seyfert galaxies. This is also the case for the two ULIRGs except Mrk 273, demonstrating that a significant portion of ULIRGs in the current *NuSTAR* sample are not really “X-ray faint” with respect to the [O IV] 26 μm flux. Since the luminosity of [O IV] 26 μm is determined by that of ionizing UV photons leaked to the NLR out of surrounding matter, it should be roughly proportional to the product of $(1 - \text{covering fraction})$ and the intrinsic AGN luminosity in the UV band. Thus, there could be two explanations for this observational fact. The first one is that the AGN in UGC 5101 is not different from those in normal Seyfert galaxies in terms of the covering fraction of surrounding matter and UV to X-ray spectral energy distribution (SED). The second one is that, in UGC 5101, *both* [O IV] 26 μm and X-ray luminosities are smaller with respect to the bolometric AGN luminosity than in normal Seyfert galaxies.

We find difficulties in the first explanation, however. The AGN bolometric luminosity converted from the 2–10 keV luminosity with the Marconi et al. (2004) relation (i.e., that for normal AGNs) turns out to be $\approx 2.6 \times 10^{44} \text{ erg s}^{-1}$ (with a bolometric correction factor of 19), corresponding to only $\approx 7\%$ of the total bolometric luminosity. This fraction is smaller than those estimated from the

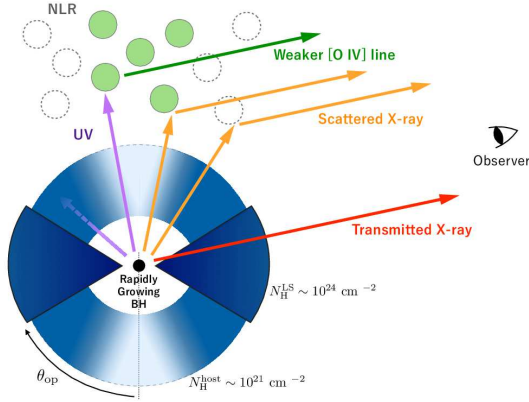


FIG. 7.— Geometry of our proposed scenario described in Section 4. The Compton-thick torus has only a moderate covering fraction. The torus-hole region is partially filled with gas and dust of $N_{\text{H}}^{\text{host}} \sim 10^{21} \text{ cm}^{-2}$. Thus, a significant fraction of ionizing UV photons from the central AGN are blocked before reaching the NLR, while X-rays are not blocked thanks to their strong penetrating power.

Spitzer spectra with diagnostics not using the NLR lines, $f_{\text{AGN}} = 52\% - 80\%$ (Armus et al. 2007) (see their Table 7) or $f_{\text{AGN}} = 14\% - 55\%$ (Veilleux et al. 2009) (see their Table 12). This implies that the SED of the AGN in UGC 5101 is X-ray under-luminous relative to the UV luminosity, which dominates the bolometric one, as compared with normal AGNs. Also, as mentioned in Section 1, the [O IV] 26 μm luminosity seems to underestimate the true bolometric AGN luminosity, implying that the total covering fraction of Compton-thick and Compton-thin matter is larger than those of normal AGNs.

We therefore consider that the second explanation would be a likely scenario for UGC 5101. Our picture, illustrated in Figure 7, is summarized as follows, even though there are large uncertainties (by a factor of a few) in the numbers. The surrounding structure consists of two parts, a Compton-thick part ($N_{\text{H}} \sim 10^{24} \text{ cm}^{-2}$) located close to the equatorial plane and a Compton-thin part ($N_{\text{H}} \sim 10^{21} \text{ cm}^{-2}$) in the torus hole region, although they may not be discrete in reality. The covering fraction of Compton-thick matter is small, which is derived from the hard X-ray spectra. The *total* covering fraction of Compton-thick and Compton-thin matter that blocks UV lights is large, which accounts for the low [O IV] 26 μm luminosity relative to the AGN bolometric luminosity. The intrinsic bolometric luminosity of the AGN is truly $L_{\text{bol}} \sim 2 \times 10^{45} \text{ erg s}^{-1}$, corresponding to $\sim 50\%$ of the total luminosity, as inferred from the IR spectra. Because the intrinsic AGN luminosity in the 2–10 keV band we determine is $L_{\text{X}} \approx 1.4 \times 10^{43} \text{ erg s}^{-1}$, the 2–10 keV to bolometric luminosity correction factor of this AGN is estimated to be $L_{\text{bol}}/L_{\text{X}} \sim 140$. This value is relatively large (i.e., the UV to X-ray SED is steep) compared with those of typical Seyferts with similar X-ray luminosities (Marconi et al. 2004), but can be expected at high Eddington rates (Vasudevan & Fabian 2007) i.e., in rapidly growing SMBHs. Thus, because both the [O IV] 26 μm and X-ray luminosities are suppressed, their ratio remains almost the same as those of normal Seyferts. Nevertheless, we argue that AGNs in many ULIRGs do not look extraordinary (i.e., extremely X-ray faint), as

suggested by recent works (e.g., Teng et al. 2015), compared with normal Seyferts. Since the strong starburst activity in the nuclear region may increase both the total covering fraction of surrounding matter and the mass accretion rate, it may not be a coincidence that a ULIRG shows a standard value of the [O IV] 26 μm to X-ray luminosity ratio.

To summarize, we have revealed the complex structure of the circumnuclear region of UGC 5101; in short, the covering fraction of the Compton-thick torus is small, while the total covering fraction of Compton-thick and Compton-thin matter is large, making the nucleus “unburied” in X-rays but “buried” in UV. This implies that, in a more realistic geometry, there is a strong contrast in the column-density distribution as a function of inclination angle, that is, matter is highly concentrated toward the equatorial plane. We point out that the nearby Compton-thick AGN NGC 4945 may have a similar circumnuclear structure to that of UGC 5101. In NGC 4945, X-ray spectral and variability properties suggest a small covering fraction of the Compton-thick torus (e.g., Itoh et al. 2008; Marinucci et al. 2012), whereas, from observations of NLR lines (e.g., Pérez-Beaupuits et al. 2011), it is inferred that the AGN is surrounded by matter with a large covering fraction. To answer the question if this is a general property of obscuring material in Compton thick AGNs, it is important to perform sensitive broadband X-ray observations for a larger sample of heavily obscured AGNs.

5. CONCLUSION

Using all available data taken with *Swift*, *NuSTAR*, *Suzaku*, *XMM-Newton*, and *Chandra*, we have presented the best quality broadband X-ray spectra of UGC 5101 covering the 0.25–100 keV band. The spectra are well reproduced by conventional analytic models or a numerical torus model for an obscured AGN. The main conclusions are summarized below.

- We detect a Compton-thick AGN with a line-of-sight column density of $N_{\text{H}}^{\text{LS}} \approx 1.3 \times 10^{24} \text{ cm}^{-2}$. The intrinsic 2–10 keV luminosity is determined to be $\approx 1.4 \times 10^{43} \text{ erg s}^{-1}$, which is ≈ 2.5 times larger than the previous estimate using only data below 10 keV.
- A weak absorption of $N_{\text{H}}^{\text{host}} \sim 10^{21} \text{ cm}^{-2}$ to the soft X-ray scattered component is required.
- A spectral fit with a smooth torus model favors a large (> 41 degrees) half opening angle of the torus. This suggests that the covering fraction of a Compton-thick part is moderate.
- The ratio between the [O IV] 26 μm line and 2–10 keV luminosities of UGC 5101 and other typical ULIRGs is found to be similar to those of normal Seyfert galaxies. Thus, a significant portion of ULIRGs are not really “X-ray faint” with respect to the [O IV] 26 μm flux.
- To reconcile these results with the large AGN contribution ($\sim 50\%$) to the total bolometric luminosity inferred by the IR spectra, a possible scenario is that (1) the AGN in UGC 5101 is surrounded not

only by Compton-thick matter located close to the equatorial plane but also by Compton-thin matter with $N_{\text{H}}^{\text{host}} \sim 10^{21} \text{ cm}^{-2}$ in the torus-hole region, and (2) it has a steep UV to X-ray SED, which is expected at a high Eddington rate. These two effects work to somewhat (but not extraordinarily) reduce the [O IV] $26 \mu\text{m}$ and X-ray luminosities, respectively, by keeping their ratio almost the same as in normal Seyfert galaxies.

- The circumnuclear structure of UGC 5101 may be similar to that of NGC 4945, where the covering fraction of a Compton-thick part is small but the total covering fraction of Compton-thick and Compton-thin parts is large.

This research has made use of the *NuSTAR* Data Analysis Software (NUSTARDAS) jointly developed by the ASI Science Data Center (ASDC, Italy) and the California Institute of Technology (Caltech, USA). Part of this work was financially supported by the Grant-in-Aid for Scientific Research 26400228 (Y.U.), 15K05030 (M.I.) and 15H02070 (Y.T.) from the Japan Society for the Promotion of Science (JSPS), and by the CONICYT-Chile grants “EMBIGEN” Anillo ACT1101 (C.R.), FONDECYT 1141218 (C.R.), and Basal-CATA PFB-06/2007 (C.R.). C.R. acknowledges support from the China-CONICYT fund.

REFERENCES

- Anders, E., & Grevesse, N. 1989, *Geochim. Cosmochim. Acta*, 53, 197
- Armus, L., et al. 2004, *ApJS*, 154, 178
- Armus, L., Charmandaris, V., Bernard-Salas, J., et al. 2007, *ApJ*, 656, 148
- Balucinska-Church, M., & McCammon, D. 1992, *ApJ*, 400, 699
- Bauer, F. E., Arévalo, P., Walton, D. J., et al. 2015, *ApJ*, 812, 116
- Boldt, E. 1987, *Observational Cosmology*, 124, 611
- Caputi, K. I., Lagache, G., Yan, L., et al. 2007, *ApJ*, 660, 97
- Eguchi, S., Ueda, Y., Terashima, Y., Mushotzky, R., & Tueller, J. 2009, *ApJ*, 696, 1657
- Fukazawa, Y., Mizuno, T., Watanabe, S., et al. 2009, *PASJ*, 61, S17
- Goncalves, A. C., Veron-Cetty, M. -P., & Veron, P. 1999, *A&AS*, 135, 437
- Goto, T., Takagi, T., Matsuhara, H., et al. 2010, *A&A*, 514, A6
- Grimm, H.-J., Gilfanov, M., & Sunyaev, R. 2003, *MNRAS*, 339, 793
- Guainazzi, M., & Bianchi, S. 2007, *MNRAS*, 374, 1290
- Güver, T., & Özel, F. 2009, *MNRAS*, 400, 2050
- Harrison, F. A., Craig, W. W., Christensen, F. E., et al. 2013, *ApJ*, 770, 103
- Ikeda, S., Awaki, H., & Terashima, Y. 2009, *ApJ*, 692, 608
- Imanishi, M., Dudley, C. C., & Maloney, P. R. 2001, *ApJ*, 558, L93
- Imanishi, M., & Maloney, P. R. 2003, *ApJ*, 588, 165
- Imanishi, M., Terashima, Y., Anabuki, N., & Nakagawa, T. 2003, *ApJ*, 596, L167
- Imanishi, M., Nakagawa, T., Ohshima, Y., et al. 2008, *PASJ*, 60, S489
- Imanishi, M., Nakanishi, K., & Kohno, K. 2006, *AJ*, 131, 2888
- Itoh, T., Done, C., Makishima, K., et al. 2008, *PASJ*, 60, S251
- Iwasawa, K., Sanders, D. B., Teng, S. H., et al. 2011, *A&A*, 529, A106
- Kalberla, P. M. W., Burton, W. B., Hartmann, D., et al. 2005, *A&A*, 440, 775
- Kawamuro, T., Ueda, Y., Tazaki, F., Ricci, C., & Terashima, Y. 2016, *ApJS*, 225, 14
- Kohno, K. 2005, in *AIP Conf. Ser.* 783, *The Evolution of Starbursts*, ed. S. Hüttemeister, E. Manthey, D. Bomans, & K. Weis (New York: AIP), 203 (astro-ph/0508420)
- Koyama, K., Tsunemi, H., Dotani, T., et al. 2007, *PASJ*, 59, 23
- Krips, M., Neri, R., Garcia-Burillo, S., Martin, S., Combes, F., Gracia-Carpio, J., & Eckart, A. 2008, *ApJ*, 677, 262
- Lonsdale, C. J., Lonsdale, C. J., Smith, H. E., & Diamond, P. J. 2003, *ApJ*, 592, 804
- Madsen, K. K., Harrison, F. A., Markwardt, C. B., et al. 2015, *ApJS*, 220, 8
- Magdziarz, P., & Zdziarski, A. A. 1995, *MNRAS*, 273, 837
- Makishima, K., Ohashi, T., Hayashida, K., et al. 1989, *PASJ*, 41, 697
- Marconi, A., Risaliti, G., Gilli, R., et al. 2004, *MNRAS*, 351, 169
- Marinucci, A., Risaliti, G., Nardini, E., et al. 2012, *American Institute of Physics Conference Series*, 1427, 141
- Mitsuda, K., Bautz, M., Inoue, H., et al. 2007, *PASJ*, 59, 1
- Murphy, E. J., Chary, R.-R., Dickinson, M., et al. 2011, *ApJ*, 732, 126
- Nandra, K., O’Neill, P. M., George, I. M., & Reeves, J. N. 2007, *MNRAS*, 382, 194
- Nardini, E., Risaliti, G., Salvati, M., et al. 2009, *MNRAS*, 399, 1373
- Noguchi, K., Terashima, Y., Ishino, Y., et al. 2010, *ApJ*, 711, 144
- Pérez-Beaupuits, J. P., Spoon, H. W. W., Spaans, M., & Smith, J. D. 2011, *A&A*, 533, A56
- Ricci, C., Ueda, Y., Koss, M. J., et al. 2015, *ApJ*, 815, L13
- Rigby, J. R., Diamond-Stanic, A. M., & Aniano, G. 2009, *ApJ*, 700, 1878
- Robson, I. 1996, *Active Galactic Nuclei* (New York: Wiley)
- Rosa-González, D., Terlevich, E., & Terlevich, R. 2002, *MNRAS*, 332, 283
- Sanders, D. B., & Mirabel, I. F. 1996, *ARA&A*, 34, 749
- Sanders, D. B., Soifer, B. T., Elias, J. H., Madore, B. F., Matthews, K., Neugebauer, G., & Scoville, N. Z. 1988a, *ApJ*, 325, 74
- Sanders, D. B., Soifer, B. T., Elias, J. H., Neugebauer, G., & Matthews, K. 1988, *ApJ*, 328, L35
- Scoville, N. Z. et al. 2000, *AJ*, 119, 991
- Smith, H. E., Lonsdale, C. J., & Lonsdale, C. J. 1998, *ApJ*, 492, 137
- Soifer, B. T. et al. 2000, *AJ*, 119, 509
- Takahashi, T., Abe, K., Endo, M., et al. 2007, *PASJ*, 59, 35
- Teng, S. H., Rigby, J. R., Stern, D., et al. 2015, *ApJ*, 814, 56
- Teng, S. H., Veilleux, S., Anabuki, N., et al. 2009, *ApJ*, 691, 261
- Ueda, Y., Eguchi, S., Terashima, Y., et al. 2007, *ApJ*, 664, L79
- Vasudevan, R. V., & Fabian, A. C. 2007, *MNRAS*, 381, 1235
- Veilleux, S., Kim, D. -C., Sanders, D. B., Mazzarella, J. M., & Soifer, B. T. 1995, *ApJS*, 98, 171
- Veilleux, S., Rupke, D. S. N., Kim, D.-C., et al. 2009, *ApJS*, 182, 628-666
- Yuan, T. -T., Kewley, L. J., & Sanders, D. B. 2010, *ApJ*, 709, 884